PAPER • OPEN ACCESS

First-principles insights into the spin-valley physics of strained transition metal dichalcogenides monolayers

View the article online for updates and enhancements.

CrossMark

PAPER

First-principles insights into the spin-valley physics of strained transition metal dichalcogenides monolayers

Paulo E Faria Junior[1],[*] ⓘ, Klaus Zollner[1] ⓘ, Tomasz Woźniak[2] ⓘ, Marcin Kurpas[3] ⓘ, Martin Gmitra[4] ⓘ and Jaroslav Fabian[1] ⓘ

1.   Institute for Theoretical Physics, University of Regensburg, 93040 Regensburg, Germany
2.   Department of Semiconductor Materials Engineering, Wrocław University of Science and Technology, 50-370 Wrocław, Poland
3.   Institute of Physics, University of Silesia, 75 Pułku Piechoty 1, 41-500 Chorzów, Poland
4.   Institute of Physics, Pavol Jozef Šafárik University in Košice, Park Angelinum 9, 04001 Košice, Slovakia
*   Author to whom any correspondence should be addressed.

E-mail: paulo-eduardo.faria-junior@ur.de

Abstract

Transition metal dichalcogenides (TMDCs) are ideal candidates to explore the manifestation of spin-valley physics under external stimuli. In this study, we investigate the influence of strain on the spin and orbital angular momenta, effective g-factors, and Berry curvatures of several monolayer TMDCs (Mo and W based) using a full *ab initio* approach. At the K-valleys, we find a surprising decrease of the conduction band spin expectation value for compressive strain, consequently increasing the dipole strength of the dark exciton by more than one order of magnitude (for $\sim 1\%$–2% strain variation). We also predict the behavior of direct excitons g-factors under strain: tensile (compressive) strain increases (decreases) the absolute value of g-factors. Strain variations of $\sim 1\%$ modify the bright (A and B) excitons g-factors by $\sim 0.3(0.2)$ for W (Mo) based compounds and the dark exciton g-factors by ~ 0.5 (0.3) for W (Mo) compounds. Our predictions could be directly visualized in magneto-optical experiments in strained samples at low temperature. Additionally, our calculations strongly suggest that strain effects are one of the possible causes of g-factor fluctuations observed experimentally. By comparing the different TMDC compounds, we reveal the role of spin–orbit coupling (SOC): the stronger the SOC, the more sensitive are the spin-valley features under applied strain. Consequently, monolayer WSe$_2$ is a formidable candidate to explore the role of strain on the spin-valley physics. We complete our analysis by considering the side valleys, Γ and Q points, and by investigating the influence of strain in the Berry curvature. In the broader context of valley- and strain-tronics, our study provides fundamental microscopic insights into the role of strain in the spin-valley physics of TMDCs, which are relevant to interpret experimental data in monolayer TMDCs as well as TMDC-based van der Waals heterostructures.

1. Introduction

Transition metal dichalcogenides (TMDCs) are versatile van der Waals materials that offer unique opportunities to explore fundamental and applied physics in (opto)electronics [1–3], (opto)spintronics [4–6], and valleytronics applications [7–10]. At the monolayer limit, the TMDCs with hexagonal crystal structure (2H polytype with D_{3h}^1 space group) are direct band gap semiconductors with electrons and holes localized at the K-points of the first Brillouin zone [11–13] and robust excitonic signatures in the optical spectra [14–18]. Furthermore, the lack of inversion symmetry of the crystal lattice, combined with heavy metal elements, imprints strong spin–orbit coupling (SOC) physics at the K-valleys by 'polarizing' the spins in the out-of-plane direction, with opposite orientation at opposite K-valleys (due to time-reversal

symmetry) [19, 20]. This spin-valley locking of electrons and holes is also reflected in the selection rules of the excitons, allowing for the selective excitation of exciton quasi-particles originating from either K or $-K$ valley [7–10].

One possible way to probe the spin-valley physics of electrons, holes, and excitons in monolayer TMDCs is using magneto-optical spectroscopy [21]. Lifting the degeneracy of K and $-K$ valleys under external magnetic field gives rise to a net (valley) Zeeman splitting, distinctly observed in the excitonic spectra, with the sign and magnitude encoded by the g-factors. In monolayer TMDCs, for instance, the typical values for the fundamental A exciton g-factor gravitate around -4, often explained in terms of orbital, spin and valley (self-rotation) contributions [22–37]. Despite the clear signature in the excitonic spectra, measuring the exciton g-factor simultaneously accounts for the electron and hole contributions, requiring additional emission peaks to reveal the independent contributions of conduction and valence bands. Fortunately, recent experimental efforts relying on multiple phonon-mediated emission peaks [33, 34] were able to disentangle the conduction and valence band g-factors. The measured values are in great agreement with state-of-the-art first-principles calculations [38–41] that properly evaluate the Bloch contribution to the band g-factors, finally establishing a connection to the vast existing knowledge in the area of III–V materials [42–52]. These new theoretical developments on g-factor calculations allow us to grasp the fundamental microscopic physics that drives the g-factors in more complex TMDC-based systems, such as van der Waals heterostructures [38, 40, 41], doping effects [53] and defect states [54] in monolayers, and bulk materials [55].

Besides the unique spin-valley physics, TMDCs are flexible materials strongly suitable for straintronics [56, 57]. Particularly, applying controllable strain in TMDCs is a very efficient way to modulate the optical emission energy of excitons by several hundreds of meV [58–63]. Furthermore, it has been shown that strain is a crucial ingredient to suppress nonradiative exciton recombination, remarkably preserving the quantum yield of the photoluminescence close to unity [64]. Conversely, strain may also arise as an undesired byproduct during the fabrication process of monolayers and van der Waals heterostructures, leading to spatially inhomogeneous strain fields that permeate the sample [65–69]. Although there have been several theoretical reports on the impact of strain on the energy level [70–73], not much is known about the microscopic impact of strain on the spin-valley physics, particularly on the spin-mixing and g-factors. Revealing the isolate impact of strain on the spin-valley physics provides fundamental insight on possible fluctuations on the spin and valley dependent properties of TMDC monolayers as well as TMDC-based van der Waals heterostructures [4, 69, 74–83]. This fundamental understanding is also relevant to the theoretical modelling of van der Waals heterostructures within first-principles, in which strain is often needed to effectively create commensurate supercells.

Here, we investigate the impact of strain on the spin-valley physics of monolayer TMDCs with hexagonal crystal structure (2H polytype). Specifically, we evaluate the spin and orbital angular momenta, effectives g-factors, and Berry curvatures of MoS_2, $MoSe_2$, $MoTe_2$, WS_2 and WSe_2 using first-principles calculations. For the K-valley, our calculations unveiled a surprising spin-mixing regime under compressive strain for the conduction band with majority of spin down. Performing a systematic symmetry analysis, we pinpoint the origin of such spin mixing to a spin-flip coupling to a higher conduction band. For the direct excitons stemming from the low energy bands at the K-valleys, namely the A, B and D (dark) excitons, our calculations reveal important trends for the Zeeman splitting: positive (negative) strain values increase (decrease) the absolute value of the g-factors. We also found that the dark exciton g-factor is the most sensitive to the applied strain and that the A and B exciton g-factors increasingly deviate from each other in the compressive strain regime. These g-factor features could be directly probed via magneto-optics in carefully controlled strained TMDCs. By connecting the g-factor trends to the dipole matrix elements, we found that, as a consequence of the spin-mixing, the dipole strength of the dark exciton can be drastically modified by orders of magnitude. Although these trends are visible in all TMDCs, the most pronounced effects are due to the larger SOC, thus making WSe_2 the most suitable candidate to study the strain modulation of spin-valley physics. We also investigate the strain effects in the Berry curvature. They show similar trends as the g-factors but are more sensitive to the applied strain. In summary, our study bridges valley- and strain-tronics of monolayer TMDCs, and are relevant not only for the interpretation of experimental studies but also provide valuable insights to model TMDC-based van der Waals heterostructures.

2. Theoretical background and computational methods

2.1. Zeeman splitting and Berry curvature

When a static magnetic field, B, is applied perpendicular to a TMDC monolayer (along the z-direction), the energy levels corresponding to Bloch states, labeled by the band index n and the wave vector $\vec{k}$, experience a Zeeman shift given by [38–41]

$$
\begin{aligned}
E_{ZS}(n,\vec{k}) &= \left[L_z(n,\vec{k}) + S_z(n,\vec{k}) \right] \mu_B B \\
&= g_z(n,\vec{k}) \mu_B B,
\end{aligned} \tag{1}
$$

with $\mu_B = e\hbar/2m_0$ being the Bohr magneton, e is the electron charge, $\hbar$ is the reduced Planck's constant and m_0 is the free electron mass.

The term $L_z(n,\vec{k})$ is the orbital angular momentum (or self-rotation) of the Bloch band and can be written as

$$
\begin{aligned}
L_z(n,\vec{k}) &= \left\langle n,\vec{k} \left| \frac{1}{\hbar} \left(r_x p_y - r_y p_x \right) \right| n,\vec{k} \right\rangle \\
&= \frac{1}{im_0} \sum_{m \neq n} \frac{P_x^{n,m,\vec{k}} P_y^{m,n,\vec{k}} - P_y^{n,m,\vec{k}} P_x^{m,n,\vec{k}}}{E(n,\vec{k}) - E(m,\vec{k})},
\end{aligned} \tag{2}
$$

with $P_\alpha^{n,m,\vec{k}} = \left\langle n,\vec{k} | p_\alpha | m,\vec{k} \right\rangle$ ($\alpha = x, y, z$), $\vec{r}$ being the position operator and $\vec{p}$ being the momentum operator. In reference [84], it was shown that this expression for the angular momentum is valid at any $\vec{k}$-point of the crystal's reciprocal space. At the band edges, this expression is equivalent to the well established perturbation theory developed in the late 1950s and extensively applied to semiconductors with diamond, zinc-blende and wurtzite crystal structures [42–51].

The term $S_z(n,\vec{k})$ reflects the spin angular momentum of the Bloch band

$$
S_z(n,\vec{k}) = \frac{g_0}{2} \left\langle n,\vec{k} | \hat{\sigma}_z | n,\vec{k} \right\rangle \approx \left\langle n,\vec{k} | \hat{\sigma}_z | n,\vec{k} \right\rangle, \tag{3}
$$

in which $g_0 \approx 2.002\,318$ is the electron spin g-factor and σ_z is the Pauli matrix. Note that in our notation the spin values given by S_z range from -1 (spin down) to 1 (spin up).

Therefore, the Zeeman energy shifts of electrons, holes, and consequently excitons, can be investigated by exploring the physical quantities $L_z(n,\vec{k})$, $S_z(n,\vec{k})$ and $g_z(n,\vec{k}) = L_z(n,\vec{k}) + S_z(n,\vec{k})$. Furthermore, because of time-reversal symmetry, the relation $O(n,-\vec{k}) = -O(n,\vec{k})$ holds for $O = L_z$, S_z and g_z.

If such monolayer TMDC is now in the presence of a static (weak) in-plane electric field, the velocity of electrons and holes acquires an additional term proportional to the Berry curvature in the out-of-plane direction [85], with distinct signatures in the Hall conductivity [86]. Besides this anomalous velocity term, the Berry curvature also influences the energy splittings of p-like excitons in TMDCs [87–89]. The expression for the Berry curvature is given by [84]

$$
\Omega_z(n,\vec{k}) = \frac{\hbar^2}{im_0^2} \sum_{m \neq n} \frac{\vec{P}_x^{n,m,\vec{k}} \vec{P}_y^{m,n,\vec{k}} - \vec{P}_y^{n,m,\vec{k}} \vec{P}_x^{m,n,\vec{k}}}{\left[E(n,\vec{k}) - E(m,\vec{k}) \right]^2} \tag{4}
$$

and resembles equation (2) for the angular momentum, except for the multiplicative constants and the power of 2 in the energy denominator. Time-reversal symmetry also applies to the Berry curvature and $\Omega_z(n,-\vec{k}) = -\Omega_z(n,\vec{k})$.

2.2. Strained crystal structure

Monolayer TMDCs under biaxial strain of a few % show a linear dependence of thickness and lattice parameters. This can be derived from the symmetry properties of the crystal [90–92] and has also been observed in fully relaxed density functional theory (DFT) calculations [73, 93]. Starting from the unstrained experimental values, biaxial strain modifies the in-plane lattice parameter, a, and the monolayer thickness, d, via the relations

$$
\begin{aligned}
a &= (1 + \varepsilon) a_0 \\
d &= (1 - 2\nu_\perp \varepsilon) d_0,
\end{aligned} \tag{5}
$$

Table 1. Structural parameters considered in the calculations. The experimental lattice parameters a_0 and d_0, given in Å, are taken from reference [19]. The values of $\nu_\perp$ for (Mo, W) (S, Se)$_2$ are extracted from reference [73] and MoTe$_2$ from reference [93].

	MoS$_2$	MoSe$_2$	MoTe$_2$	WS$_2$	WSe$_2$
a_0	3.160	3.289	3.522	3.153	3.282
d_0	3.170	3.335	3.604	3.140	3.340
$\nu_\perp$	0.3385	0.3502	0.3700	0.3567	0.3646

in which a_0 and d_0 are the unstrained values, ε is the applied biaxial strain and $\nu_\perp$ is the so called Poisson ratio, related to the elastic constants of the crystal structure [93]. A summary of the lattice parameters and Poisson ratios used in the calculations are given in table 1. We emphasize that the experimental values of a_0 and d_0 are nicely reproduced by previous calculations, as well as the linear dependence of the thickness d with respect to the applied strain, as shown in reference [73].

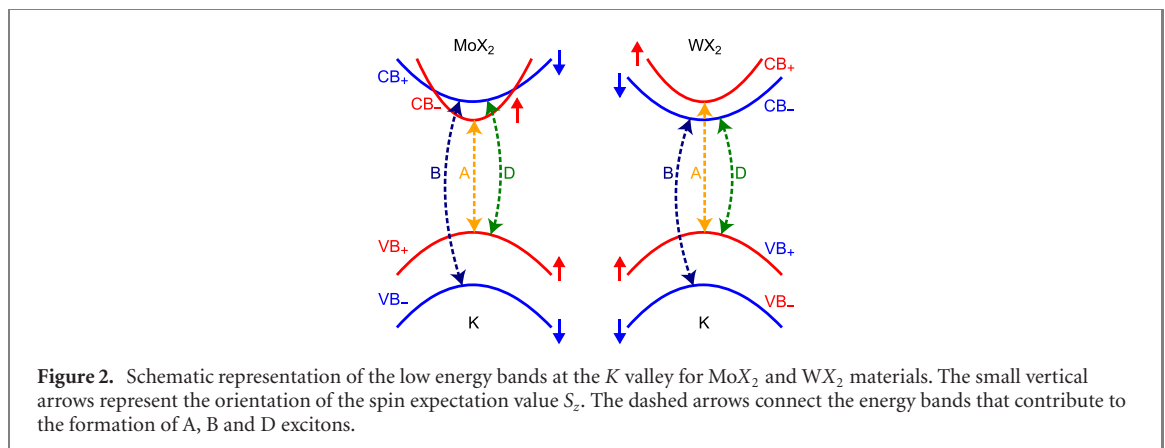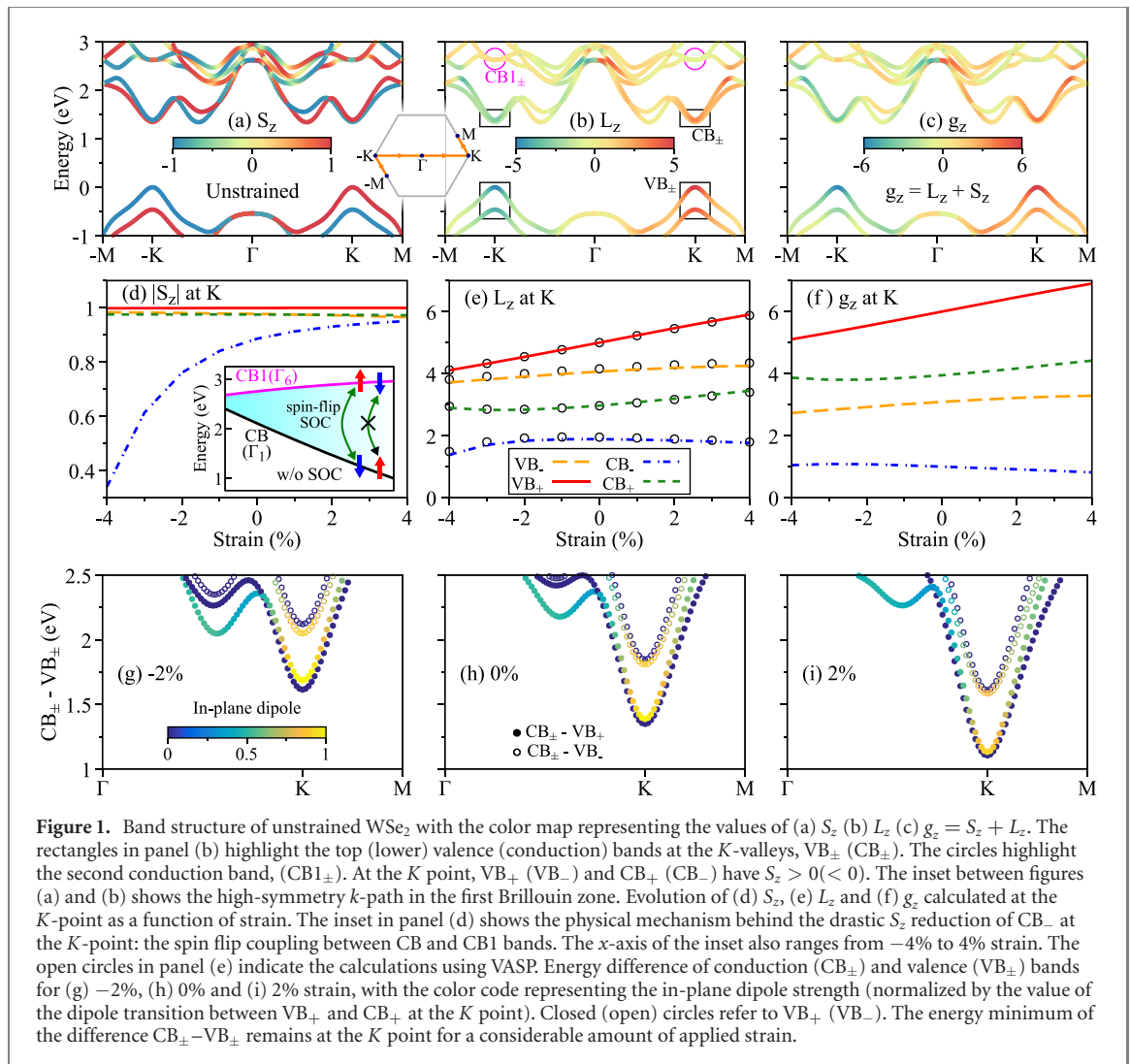### 2.3. First-principles calculations

The first-principles calculations are performed using the WIEN2k package [94], which implements a full potential all-electron scheme employing augmented plane wave plus local orbitals (APW + lo) method. The strained TMDC crystal structure is generated using the atomic simulation environment python package [95] with a vacuum spacing of 16 Å to avoid interaction among the periodic replicas. We used the Perdew–Burke–Ernzerhof (PBE) exchange–correlation functional [96], a Monkhorst–Pack k-grid of 15×15 and self-consistent convergence criteria of 10^{-6} e for the charge and 10^{-6} Ry for the energy. We considered a core–valence separation energy of -6 Ry, atomic spheres with orbital quantum numbers up to 10 and the plane-wave cutoff multiplied by the smallest atomic radii is set to 9. For the inclusion of SOC, core electrons are considered fully relativistically whereas valence electrons are treated in a second variational step [97], with the scalar-relativistic wave functions calculated in an energy window of -10 to 10 Ry. The chosen energy window thus provides more than 1000 bands, which are crucial for a proper convergence of the angular momentum, $L_z(n, \vec{k})$ given in equation (2), as shown in references [38, 40].

For comparison and to emphasize the generality of our results, we also performed the angular momentum calculations using the plane-wave based DFT code Vienna *ab initio* simulation package (VASP) [98]. We used the PBE exchange–correlation functional and the projector augmented wave method [99]. An energy cutoff of 300 eV and a 9×9 k-mesh were chosen after careful convergence tests. The k-space integration was carried out with a Gaussian smearing method using an energy width of 0.05 eV. The momentum matrix elements in equation (2) were obtained from the wave function derivatives that are calculated within the density functional perturbation theory [100]. Furthermore, in order to converge the angular momentum calculations, more than 700 bands were used.

3. Spin-mixing, angular momentum and *g*-factors at the *K* valleys

The low energy physics in TMDCs can be traced to the conduction and valence band extrema located at the K-valleys of the first Brillouin zone [11–13]. Let us initially focus on WSe$_2$ and understand the overall behavior of S_z, L_z and g_z without strain. In figures 1(a)–(c) we show the calculated band structure for unstrained WSe$_2$ along the high-symmetry k-path $-M \rightarrow -K \rightarrow \Gamma \rightarrow K \rightarrow M$ with the color code representing the calculated values of S_z, L_z and g_z, respectively. The lowest conduction bands, CB$_\pm$, and highest valence bands, VB$_\pm$, are indicated in figure 1(b), with the subindex $+$ or $-$ referring to the energetic band ordering. These are the important energy bands that contribute to the formation of the A and B ('bright') excitons, with in-plane optical selection rules, and of the D ('dark') exciton, with out-of-plane optical selection rule [14, 15, 33, 34, 36, 101–103]. The relevant low energy bands that contribute to the formation of the A, B and D excitons are sketched in figure 2. Regarding spin, the values of S_z are rather homogeneous for CB$_\pm$ and VB$_\pm$ along the high-symmetry k-path, i.e., the bands are highly spin polarized with $|S_z| \sim 1$. In contrast to S_z, L_z shows a larger dispersion with the highest values located at the K-valleys, a signature of the massive Dirac nature of the system [13, 104]. Particularly at the K ($-K$) point, L_z is positive (negative) for both CB$_\pm$ and VB$_\pm$. Adding L_z and S_z allows us to look at the g-factors of the Bloch bands, g_z, the key ingredient that controls the Zeeman shift (see equation (1)). The color plot in figure 1(c) for g_z shows a very similar structure to L_z, but with smaller amplitudes for the bands with $S_z < 0$. However, at the K ($-K$) valleys, the values of g_z remain positive (negative), since $|L_z| > |S_z|$.

In order to understand the impact of strain on S_z, L_z and g_z, let us have a closer look at the CB$_\pm$ and VB$_\pm$ bands directly at the K valley. In figure 1(d), we show the calculated values of $|S_z|$ as function of the

Figure 1. Band structure of unstrained WSe$_2$ with the color map representing the values of (a) S_z (b) L_z (c) $g_z = S_z + L_z$. The rectangles in panel (b) highlight the top (lower) valence (conduction) bands at the K-valleys, VB$_\pm$ (CB$_\pm$). The circles highlight the second conduction band, (CB1$_\pm$). At the K point, VB$_+$ (VB$_-$) and CB$_+$ (CB$_-$) have $S_z > 0(< 0)$. The inset between figures (a) and (b) shows the high-symmetry k-path in the first Brillouin zone. Evolution of (d) S_z, (e) L_z and (f) g_z calculated at the K-point as a function of strain. The inset in panel (d) shows the physical mechanism behind the drastic S_z reduction of CB$_-$ at the K-point: the spin flip coupling between CB and CB1 bands. The x-axis of the inset also ranges from -4% to 4% strain. The open circles in panel (e) indicate the calculations using VASP. Energy difference of conduction (CB$_\pm$) and valence (VB$_\pm$) bands for (g) -2%, (h) 0% and (i) 2% strain, with the color code representing the in-plane dipole strength (normalized by the value of the dipole transition between VB$_+$ and CB$_+$ at the K point). Closed (open) circles refer to VB$_+$ (VB$_-$). The energy minimum of the difference CB$_\pm$–VB$_\pm$ remains at the K point for a considerable amount of applied strain.

Figure 2. Schematic representation of the low energy bands at the K valley for MoX_2 and WX_2 materials. The small vertical arrows represent the orientation of the spin expectation value S_z. The dashed arrows connect the energy bands that contribute to the formation of A, B and D excitons.

applied strain. Because of the complex nature of SOC in crystals, spins are allowed to mix and generally $|S_z| \neq 1$. That is indeed the case, even at zero strain, for CB$_\pm$ and VB$_\pm$ bands. Surprisingly, CB$_-$ has the largest spin mixing and shows a drastic reduction of S_z for compressive strain values, originating from a particular symmetry-allowed spin-flip SOC to a higher conduction band, labeled here as CB1 and highlighted with a circle in figure 1(b). The irreducible representations of the relevant energy bands are given in the appendix A and the symmetry-allowed couplings for CB are discussed in the appendix B.

The spin-mixing that reduces the value of S_z does not introduce any in-plane spin component, a peculiar feature of 2D materials with out-of-plane mirror symmetry. This feature has important consequences to the Elliot–Yafet spin relaxation mechanism [20]. This drastic reduction of S_z is a general feature we observed in all 2H TMDCs (see appendix C). Furthermore, since spins are quite robust at the top

Table 2. Band *g*-factors at zero strain. Comparison of calculated and experimental *g*-factors for VB$_-$, VB$_+$, CB$_-$, and CB$_+$ energy bands for WSe$_2$ and WS$_2$ compounds. The term spin-valley-orbital refers to the earlier theoretical attempts to compute *g*-factors in TMDCs.
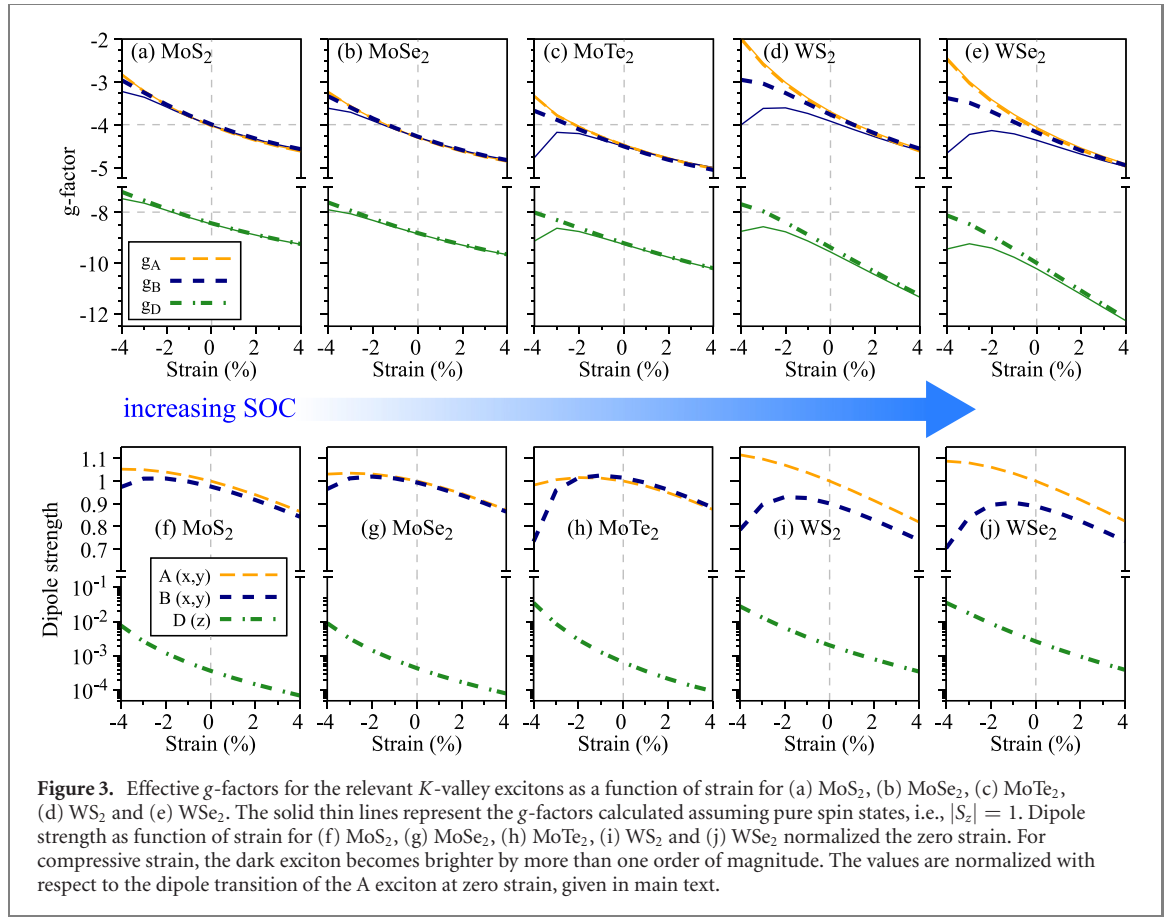
		VB$_-$	VB$_+$	CB$_-$	CB$_+$
	Exp.: Robert *et al* [33]	2.81 ± 0.5	6.1 ± 0.1	0.86 ± 0.1	3.84 ± 0.1
	Theory: this study	3.09	6.00	1.00	3.95
	Theory: Woźniak *et al* [38]	3.00	5.81	0.87	3.91
WSe$_2$	Theory: Deilmann *et al* [39]	3.15	5.91	0.99	3.97
	Theory: Förste *et al* [40]		5.90	0.90	3.9
	Theory: Xuan *et al* [41]	3.17	5.86	0.90	3.81
	Theory: spin-valley-orbital [25]		3.50	1.50	5.50
	Exp.: Zinkiewicz *et al* [34]	3.08 ± 0.08	5.47 ± 0.09	1.08 ± 0.08	3.70 ± 0.10
	Theory: this study	3.28	6.09	1.39	4.22
WS$_2$	Theory: Zinkiewicz *et al* [34]	2.79	5.23	0.87	3.45
	Theory: Woźniak *et al* [38]	3.29	6.03	1.31	4.20
	Theory: Deilmann *et al* [39]	3.29	5.94	1.35	4.21

of the valence band ($|S_z| \approx 1$) but the conduction band electrons have mixed spins, one would expect different signatures in the spin dynamics of electrons and holes, even at zero strain. Interestingly, recent experimental studies [105–107] have already reported much longer (spin) polarization relaxation times for holes than electrons. Although the physical mechanism is not fully understood, the reduced electron (spin) polarization relaxation is typically attributed to intervalley spin scattering mechanisms assuming electronic states without any spin-mixing. Our results suggest that spin-mixing of conduction band electrons might be an important ingredient to fully understand the dynamics observed in experiments and that it can be tuned with strain. We emphasize that despite the tunability of the spin-mixing introduced by the biaxial strain, the hexagonal symmetry of the TMDC lattice is maintained, and thus the irreducible representations of the energy bands remain unaffected (see appendix A). Consequently, there is no change in the valley optical selection rules.

Our calculated values of S_z as function of strain are also relevant to theoretical investigations of proximity effects in van der Waals heterostructures [4–6, 74, 78, 108, 109]. To create commensurate supercells with periodic boundary conditions required in *ab initio* calculations, it is often necessary to strain the materials involved. If the proximity effects originate from the conduction band of TMDCs, our results show that negative strain values can influence the final results via the drastic change of S_z. From this perspective, it is desirable to apply positive strain for TMDCs, which has a less drastic impact on the S_z of CB$_-$, particularly in W-based materials.

Let us now turn to the calculated values of L_z as a function of the biaxial strain, presented in figure 1(e). As an overall trend, the value of L_z for each band increases (decreases) as strain increases (decreases). Furthermore, the calculated values of L_z are consistent regardless of the DFT code/approach used (WIEN2k with lines and VASP with open circles), in line with recent studies [38–41]. Adding S_z and L_z we then obtain the values of g_z as a function of the strain, shown in figure 1(e). For the range of strain analyzed, the *g*-factors at the *K* valley are positive, with the largest variation arising from VB$_+$. Particularly for WSe$_2$ and WS$_2$, recent experiments [33, 34] were able to identify the *g*-factor of these low energy bands separately, which allows a direct comparison with the calculated band *g*-factors. In table 2, we compare our calculated *g*-factors with the experimentally determined values and other available calculations. For WSe$_2$, the comparison with the early spin-valley-orbital picture is also available, in which the valley *g*-factor was not properly converged and the pure atomistic angular momenta was then added to it. In summary, the recent developments [38–41] for *g*-factors calculations from first-principles provide a remarkable agreement to the experimentally determined band *g*-factors. To complete our analysis, in appendix C we present the strain dependence of S_z, L_z, and g_z for all studied 2H TMDCs (MoS$_2$, MoSe$_2$, MoTe$_2$, WS$_2$, and WSe$_2$) and, in appendix D, we explicitly provide the values of S_z, L_z, and g_z at zero strain. Additionally, we show in appendix E the band *g*-factors of WSe$_2$ and WS$_2$ calculated with a scissor shift to the band gap to compare with the experimental *g*-factor values discussed in table 2.

One possibility to probe the strain-induced changes of g_z at the *K* valleys is looking at the excitonic signatures in TMDCs. The only requirement is that the excitonic states should remain localized at the band edges of the *K*-valleys under strain. Within the formalism of the effective Bethe–Salpeter equation for excitons [54, 73, 101, 110–113], a minimum in the energy difference of conduction and valence bands is a crucial ingredient to host direct excitons. In figures 1(g)–(i) we present the energy difference of CB$_\pm$ and VB$_\pm$ for -2%, 0% and 2% strain, with the color code representing the squared value of the in-plane dipole matrix element (normalized with respect to the value at zero strain). Our calculations show that this energy

Figure 3. Effective *g*-factors for the relevant *K*-valley excitons as a function of strain for (a) MoS$_2$, (b) MoSe$_2$, (c) MoTe$_2$, (d) WS$_2$ and (e) WSe$_2$. The solid thin lines represent the *g*-factors calculated assuming pure spin states, i.e., $|S_z| = 1$. Dipole strength as function of strain for (f) MoS$_2$, (g) MoSe$_2$, (h) MoTe$_2$, (i) WS$_2$ and (j) WSe$_2$ normalized the zero strain. For compressive strain, the dark exciton becomes brighter by more than one order of magnitude. The values are normalized with respect to the dipole transition of the A exciton at zero strain, given in main text.

minimum still remains at the *K*-valley under considerable amount of applied strain and, consequently, the *K*-points are interesting valley Zeeman and exciton hotspots that can be easily accessed via magneto-optical spectroscopy experiments [21].

4. Direct excitons at the *K*-valleys: *g*-factor renormalization and dark-exciton brightening

We have established that under strain the *K*-valleys remain important hotspots (interesting points) for spin, valley Zeeman and exciton physics. As a consequence, the optical signature of the strain effects can be directly probed via the exciton *g*-factors. Based on the selection rules for the optical transitions involving CB$_\pm$ and VB$_\pm$, the *g*-factors for A, B and D excitons are written as

$$g_A = 2\big[g_z(\mathrm{CB}_{-(+)}, K) - g_z(\mathrm{VB}_+, K)\big]$$
$$g_B = 2\big[g_z(\mathrm{CB}_{+(-)}, K) - g_z(\mathrm{VB}_-, K)\big]$$
$$g_D = 2\big[g_z(\mathrm{CB}_{+(-)}, K) - g_z(\mathrm{VB}_+, K)\big], \tag{6}$$

for Mo(W)-based TMDCs. The factor 2 that appears in equation (6) is due to time-reversal symmetry properties of S_z and L_z (see section 2.1). Note that if the spin-mixing given by S_z is neglected, i.e. $|S_z| = 1$, the *g*-factor of A and B excitons is reduced to $g = 2[L_z(n_c, K) - L_z(n_v, K)]$, in which n_c and n_v are the conduction and valence bands that spawn the excitonic state. In figure 2 we present a sketch of the relevant bands that contribute to the formation of the A, B and D excitons. We note that optical transitions from VB$_-$ to CB$_{+(-)}$ in Mo(W) compounds are forbidden by symmetry and also confirmed by our first principles calculations.

The direct exciton *g*-factors, g_A, g_B and g_D as function of the strain are presented in figures 3(a)–(e) for all the studied TMDCs. We found that the *g*-factors become more negative under tensile (positive) strain and less negative under compressive (negative) strain. This is a consistent trend observed for all studied TMDCs, with the particular slopes being controlled by the strength of SOC. Particularly, the dark exciton *g*-factor, g_D, is much more sensitive to strain effects than the bright A and B exciton *g*-factors, g_A and g_B. Additionally, one peculiar feature that arises for negative strain values is the 'splitting' of g_A and g_B, and it is

Table 3. Direct exciton g-factors g_A, g_B and g_D at zero strain for all studied TMDCs. The experimental errors associated to the g-factors typically range from 0.05 to 0.5.

		MoS$_2$	MoSe$_2$	MoTe$_2$	WS$_2$	WSe$_2$
g_A	Here	-4.03	-4.30	-4.48	-3.74	-4.12
	Theory	$-3.68^a, -4.24^b$	$-3.82^a, -4.58^b$	$-3.96^a, -4.86^b$	$-3.66^a, -3.46^b$ -3.56^r	$-3.80^a, -3.88^b$ $-4.0^c, -4.1^d$
	Exp.	$-1.27^e, -1.8^f$ $-1.7^g, -1.9^g$ $-2.9^h, -3.0^h$ $-3.6^h, -3.8^h$ $-4.0^i, -4.6^j$	$-3.8^{k,l}, -4.0^f$ $-4.1^m, -4.2^{n,o}$ $-4.3^{h,p}, -4.4^j$	$-4.3^q, -4.6^h$ $-4.7^q, -4.8^{o,q}$	$-3.5^r, -3.6^s$ $-3.7^n, -3.94^{i,t}$ $-4.0^{h,n}, -4.25^u$ $-4.3^v, -4.35^w$	$-1.57^x, -2.86^x$ $-3.2^y, -3.6^z$ $-3.7^{l,aa}, -3.8^o$ $-4.0^{ab}, -4.02^{ac}$ $-4.05^{n,ad}, -4.1^{ae}$ $-4.2^{af,ag}, -4.25^{ah}$ $-4.3^{n,ai}, -4.37^{aj}$ $-4.4^{ak}, -4.5^{al}$ $-4.52^{aj}, -4.6^{ac}$
g_B	Here	-3.99	-4.28	-4.51	-3.76	-4.18
	Theory	$-3.70^a, -4.36^b$	$-3.88^a, -4.7^b$	$-4.02^a, -5.0^b$	$-3.96^a, -3.88^b$	$-4.26^a, -4.32^b$
	Exp.	-4.3^j	-4.2^n	-3.8^q	$-3.99^i, -4.9^n$	-3.9^n
g_D	Here	-8.43	-8.82	-9.22	-9.38	-10.00
	Theory	$-8.12^a, -8.68^b$	$-8.36^a, -9.14^b$	$-8.7^a, -9.64^b$	$-9.44^a, -9.18^b$ -8.73^r	$-9.88^a, -9.84^b$ $-10.1^c, -9.92^d$
	Exp.	-6.5^f	-8.6^f		$-8.9^r, -9.3^s$	$-9.1^{am}, -9.3^{aa}$ $-9.3^{an}, -9.4^{ah}$ $-9.5^{ak}, -9.6^{ag}$ $-9.9^{ao}, -10.2^{al}$

[a] Reference [38].
[b] Reference [39].
[c] Reference [40].
[d] Reference [41].
[e] Reference [116].
[f] Reference [35].
[g] Reference [117].
[h] Reference [32].
[i] Reference [28].
[j] Reference [118].
[k] Reference [23].
[l] Reference [26].
[m] Reference [22].
[n] Reference [119].
[o] Reference [120].
[p] Reference [115].
[q] Reference [121].
[r] Reference [34].
[s] Reference [122].
[t] Reference [123].
[u] Reference [29].
[v] Reference [124].
[w] Reference [30].
[x] Reference [25].
[y] Reference [125].
[z] Reference [126].
[aa] Reference [127].
[ab] Reference [27].
[ac] Reference [114].
[ad] Reference [128].
[ae] Reference [40].
[af] Reference [31].
[ag] Reference [37].
[ah] Reference [36].
[ai] Reference [129].
[aj] Reference [24].
[ak] Reference [130].
[al] Reference [33].
[am] Reference [131].
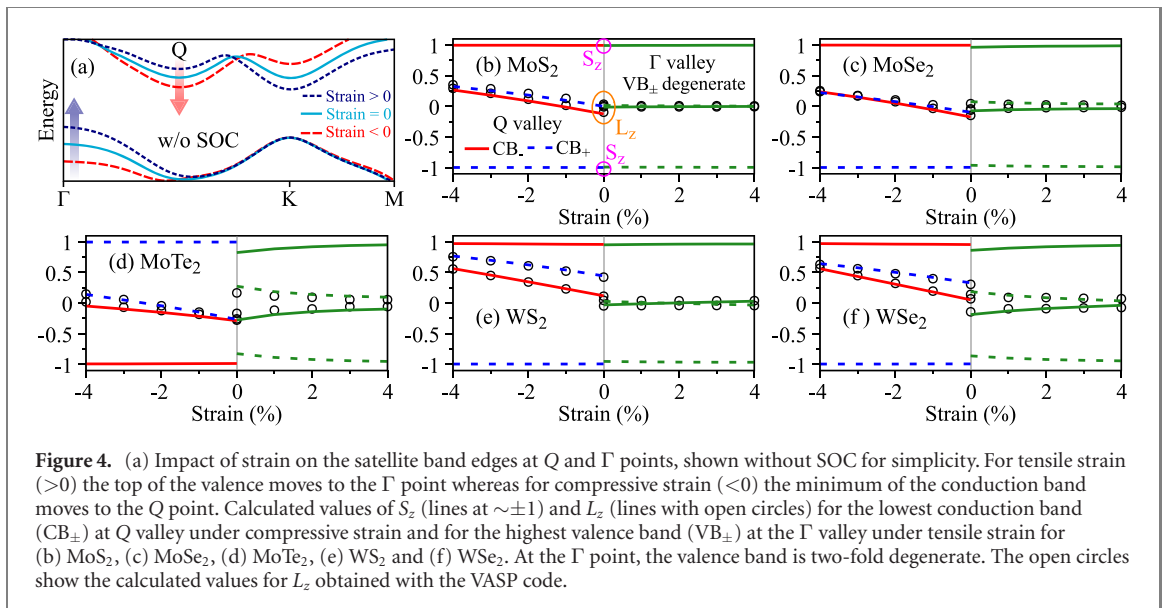[an] Reference [126].
[ao] Reference [132].

more pronounced in W-based materials due to the larger SOC. We also show for comparison the calculated *g*-factors neglecting the spin-mixing in S_z, i.e., we fix $|S_z| = 1$ for $CB_{\pm}$ and $VB_{\pm}$. While this looks a reasonable approximation for positive strain values, there are large differences introduced for negative strain values, i.e., in the strong spin-mixing regime (see figure 1(d)). Essentially, our results firmly indicate that not only the orbital contribution but also the spin-mixing strongly influence the *g*-factors in compressive strain regimes. Furthermore, our calculations suggest that strain is one of the sources of uncertainties and fluctuations in the measured *g*-factors, likely due to inhomogeneities in the fabrication process of the samples (exfoliation, stamping, encapsulation, annealing, etc). For instance, a strain variation of $\sim$1% modify the A and B bright excitons *g*-factors by $\sim$0.3 (0.2) for W (Mo) based compounds and the dark exciton *g*-factors by $\sim$0.5 (0.3) for W (Mo) compounds. These values are consistent with the experimentally available fluctuations found for bright and dark excitons in several TMDCs. In table 3, we collect the calculated *g*-factors for A, B and D excitons for all studied TMDCs at zero strain and provide a thorough comparison with the available values found in the literature from other theoretical calculations and experimental measurements.

Experimental studies combining magneto-optics and strained TMDCs are rather scarce in the literature [114, 115] and only investigate the tensile (positive) strain regime. For instance, Mitioglu *et al* [114] studied the A exciton *g*-factor at $T = 4.2$ K in WSe$_2$ monolayers under uniaxial strain by analyzing different samples (very likely with different doping levels, since the exciton/trion ratio also changes). This uniaxial strain introduces a splitting of the exciton peak, yielding two distinct *g*-factors, both less negative when compared to nominally unstrained values. Covre *et al* [115] studied the A exciton *g*-factor at $T = 4$ K in a MoSe$_2$ monolayer bubble with non-uniform strain regions, in which the carrier concentration and the dielectric environment were also changing. They observed that the A exciton *g*-factor increases its magnitude but to a value larger than the theoretical calculations, suggesting a strong influence of the other effects present in the sample. Therefore, we suggest that the predicted *g*-factor behavior revealed by our calculations (cf figure 3) could be more suitably observed in controlled strained TMDC samples at low temperatures with nearly-fixed doping levels and dielectric environments. On one hand, by using magneto-optical techniques such as absorption, reflectance or transmittance, one would have direct and isolated access to bright A and B excitons. On the other hand, dark excitons are easily probed via photoluminescence, even though using this technique could also trigger the influence of additional excitonic complexes. Nevertheless, since the dark exciton *g*-factors are the most sensitive to strain (see figures 3(a)–(e)), we speculate that if doping effects and the dielectric environment remain nearly constant, the isolated impact of strain can be revealed. Furthermore, the compressive strain regime remains completely unexplored in magneto-optical experiments. We note that, even if other effects are competing with strain in real samples, our results provide the isolated impact of strain on the energy bands and exciton *g*-factors, which are important building blocks for more sophisticated models.

Although the *g*-factors require a careful convergence with respect to the number of energy bands (see appendix F), due to L_z given by equation (2), we can qualitatively understand the 'splitting' of g_A and g_B by looking at the dipole strength, i.e., $P^2 = \left| \langle v, K | \vec{p} \cdot \hat{\epsilon} | c, K \rangle \right|^2$ with $\hat{\epsilon}$ being the light polarization unit vector (in-plane for A and B excitons and out-of-plane for D excitons). The behavior of the dipole strength as a function of strain for all studied TMDCs is summarized in figures 3(f)–(j). The plotted values are normalized by the dipole strength at zero strain for the A exciton transition. Particularly, $|P| = 5.30$ eV Å for MoS$_2$, $|P| = 4.65$ eV Å for MoSe$_2$, $|P| = 3.81$ eV Å for MoTe$_2$, $|P| = 6.64$ eV Å for WS$_2$ and $|P| = 5.87$ eV Å for WSe$_2$. Under compressive strain, the dipole strength for A and B excitons deviate from each other, the same trend observed for g_A and g_B.

Additionally, the dipole strength analysis reveals a remarkable feature of the dark excitons. Their transition amplitude changes by orders of magnitude under strain. Particularly, for compressive strain the dark excitons get brighter (but still only active with out-of-plane selection rules). This feature is intimately connected to the spin-mixing of $CB_{+(-)}$ in Mo (W) compounds. As we have shown, for negative strain, the spin expectation value, S_z, of the conduction band involved in the dark exciton formation becomes less negative (the spin-mixing increases) and more equal to the corresponding S_z value of the valence band. This strain-induced renormalization of S_z leads to a massive increase of the dipole transition amplitude and a brightening of the dark exciton. Although different mechanisms were proposed to brighten the dark exciton [133, 134] no systematic analysis of the dipole matrix elements was performed using first-principles calculations as we have shown here. Therefore, combining these different mechanisms could provide even more efficient ways of brightening dark exciton species in 2H TMDCs.

As a final remark, we would also emphasize the role of SOC in the *g*-factors and dipole matrix elements. By conveniently ordering the TMDC compounds as MoS$_2$, MoSe$_2$, MoTe$_2$, WS$_2$ and WSe$_2$ (from left to right in figure 3), we are able to appreciate the role of SOC (motivated by the strength of the CB and VB splittings, given in table D1). It is important to emphasize that SOC is a multi-faceted phenomena that

Figure 4. (a) Impact of strain on the satellite band edges at Q and Γ points, shown without SOC for simplicity. For tensile strain (>0) the top of the valence moves to the Γ point whereas for compressive strain (<0) the minimum of the conduction band moves to the Q point. Calculated values of S_z (lines at $\sim\pm1$) and L_z (lines with open circles) for the lowest conduction band (CB$_\pm$) at Q valley under compressive strain and for the highest valence band (VB$_\pm$) at the Γ valley under tensile strain for (b) MoS$_2$, (c) MoSe$_2$, (d) MoTe$_2$, (e) WS$_2$ and (f) WSe$_2$. At the Γ point, the valence band is two-fold degenerate. The open circles show the calculated values for L_z obtained with the VASP code.

controls not only the splitting of the energy bands but also their spin expectation value [20]. As a direct consequence of SOC in TMDCs, the dipole strength of the dark exciton increases as SOC increases. For instance, it is approximately one order of magnitude larger in WSe$_2$ than in MoS$_2$ at zero strain (see figures 3(f) and (j)). We suggest here that the dark exciton g-factor is the most likely candidate to reveal the SOC trends since it couples the top of the valence band (VB$_+$) with value of S_z nearly 1, and the conduction band with $S_z < 1$ that is strongly affected by the spin mixing (CB$_+$ in Mo-based and CB$_-$ in W-based TMDCs). This trend of the SOC strength is clearly visible for the calculated values of g_D at zero strain (cf table 3), with MoS$_2$ (WSe$_2$) yielding the smallest (largest) value of $|g_D|$. Interestingly, recent available experimental values of g_D in nominally unstrained MoS$_2$, MoSe$_2$, WS$_2$ and WSe$_2$ samples seem to nicely support our findings. We note that g_D is more sensitive to the scissor shift in comparison with g_A and g_B (see appendix E).
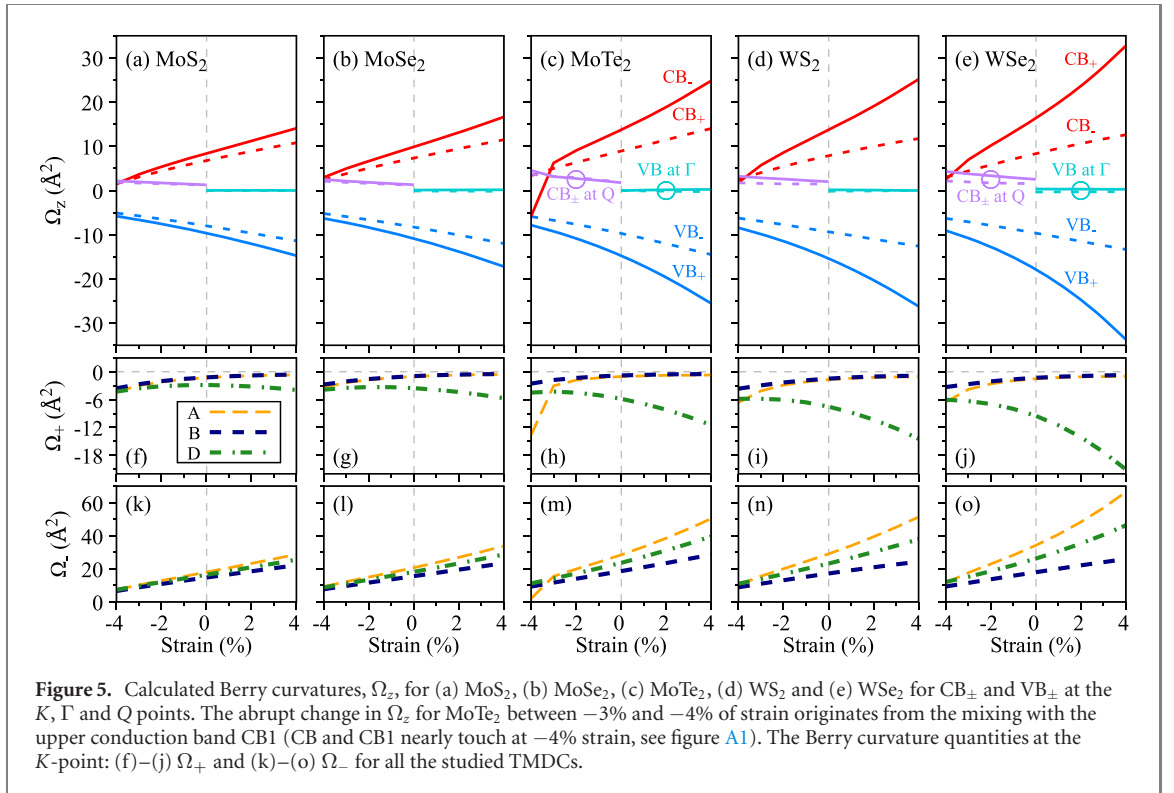
5. Spin and orbital angular momentum at Γ and Q points

Up until this point, we have looked at the strain effects on the spin, angular momentum and g-factors directly at the K valleys. However, strain acts differently on the k-points of the band structure, being capable of altering the conduction and valence band ordering [61, 70, 71, 73, 135–139]. In figure 4(a) we show the schematic effect of strain on the lowest energy bands of a TMDC (without SOC). For positive strain values, the top of the valence band moves from the K to the Γ point, while the minimum of the conduction band still remains at the K point. On the other hand, for negative strain values the minimum of the conduction band moves from K to Q (or Λ) point, while the maximum of the valence band remains at the K point. Interestingly, the interplay of conduction and valence bands from different k-points can give rise to k-momentum indirect excitons, that can be triggered in TMDCs because of the different strain rates of direct and indirect transitions [61, 73, 135–139]. We focus here on understanding the basic features of the spin and angular momentum of the energy bands at the Q and Γ points.

We summarize our findings in figures 4(b)−(f) for all the TMDCs considered in this study. For negative (positive) strain values we present S_z and L_z for the conduction (valence) band at the Q (Γ) point. Although S_z remains quite polarized ($|S_z| \sim 1$) for the states at Q and Γ points, L_z is quite quenched when compared to some of the values obtained for the K valley (see figure 1(f)). Pictorially, we can understand this reduction of L_z by recognizing that, as we move away from the K valleys, there is an increased interplay (mixture) of several atomic orbitals that leads to the reduction of L_z. In some cases, L_z is quite small and essentially negligible, such as in MoS$_2$ and WS$_2$ at the Γ point for the whole tensile strain range considered. In fact, these small and almost negligible values of L_z provide interesting opportunities to indirectly investigate the spin-valley physics at the K valley. Since the spins at Q and Γ points are well defined, the indirect g-factors are mainly ruled by the g-factor of the K valley band.

6. Berry curvature under strain

In order to complement our analysis of the spin-valley physics in TMDCs under strain, we investigate the Berry curvature, Ω_z, of the low energy bands, namely CB$_\pm$ and VB$_\pm$ at the K-valley, VB at the Γ-point and

Figure 5. Calculated Berry curvatures, Ω_z, for (a) MoS$_2$, (b) MoSe$_2$, (c) MoTe$_2$, (d) WS$_2$ and (e) WSe$_2$ for CB$_\pm$ and VB$_\pm$ at the K, Γ and Q points. The abrupt change in Ω_z for MoTe$_2$ between -3% and -4% of strain originates from the mixing with the upper conduction band CB1 (CB and CB1 nearly touch at -4% strain, see figure A1). The Berry curvature quantities at the K-point: (f)−(j) Ω_+ and (k)−(o) Ω_- for all the studied TMDCs.

CB$_\pm$ at the Q-point. In general, the Berry curvature and the angular momentum are not simply connected by a multiplicative constant (see equations (2) and (4)), as is typically the case when using the effective Dirac model [13, 88, 104]. Additionally, effective models may often lack the ingredients to probe the nuances of the relevant bands, besides being often restricted to the K-valley physics [140].

In figures 5(a)−(e) we show the calculated values of the Berry curvature under strain for all studied TMDCs. Similarly to the trends observed in L_z at the K-valley (figure 1(c)), the values of Ω_z also increase (decrease) for tensile (compressive) strain, however, they are more sensitive to strain effects than L_z, because of the quadratic energy term in the denominator in equation (4). Interestingly, experiments in MoS$_2$ monolayer under uniaxial strain [141] have shown signatures of increasing Berry curvature dipole, which depends on the derivative of the Berry curvature and on the integration around the Fermi levels. We note that, at zero strain, our calculated values are in excellent agreement with previous reports [13, 41, 140] (see table D5 for the specific values and comparison). As we move away from the K valleys, the Berry curvature drastically decreases but does not necessarily vanish, leading to nonzero values of Ω_z for CB$_\pm$ at the Q-point. At the Γ-point, however, Ω_z is essentially negligible (~ 0.1) when compared to the values at the K-valley. In fact, these abrupt changes in Ω_z from K-valley to Γ/Q points may provide distinct signatures in the Hall conductivity of electron or hole doped systems [13, 142, 143] if the strain value triggers the direct to indirect band gap transition. Furthermore, our calculated values of Ω_z at K, Γ and Q points might also be relevant for multilayer TMDC systems where the band edges shift from the K-valley to the Γ/Q points [11, 12]. We also note that the effect of SOC also follows the trends we observed in the g-factors, i.e., Ω_z shows bigger changes for TMDC compounds with stronger SOC.

The contribution of the Berry curvature for individual bands can also play an important role in the context of excitons [144, 145]. While the sum of Ω_z from conduction and valence bands influences the center-of-mass motion of the excitons, the difference of Ω_z influences the relative motion of the electron and the hole within the exciton, i.e., the internal structure of the exciton. For example, it has been shown that the splitting of 2p-like excitons in TMDCs is directly proportional to the difference of Ω_z from conduction and valence bands [87, 88]. Let us then focus on the K-valley physics and define the contributions $\Omega_\pm$ as

$$\Omega_\pm = \Omega_z(c, K) \pm \Omega_z(v, K), \qquad (7)$$

in which c and v are the conduction and valence bands, respectively, that constitute the exciton state, particularly the A, B and D excitons (see sections 3 and 4).

We show the calculated values of $\Omega_\pm$ in figures 5(f)−(o) for all studied TMDCs as function of the strain. Even at zero strain, Ω_+ for A and B excitons does not vanish (as one would obtain from the typical massive Dirac model [13, 104]), however, it does approach zero as the value of strain increases (tensile strain). On

the other hand, Ω_+ for D excitons increases as tensile strain is applied. Regarding the contribution of Ω_- to the internal structure of exciton states, we found that it increases (decreases) as tensile (compressive) strain is applied. Furthermore, the amplitude of Ω_- is larger for the A exciton, followed by the D exciton and then the B exciton. Since these changes of Ω_- due to strain directly reflect the splitting of 2p-like excitons, they could be probed experimentally using two-photon optical spectroscopy, as suggested in reference [87].

7. Conclusions

In this study, we investigated the spin-valley physics of TMDCs under biaxial strain using first-principles calculations. We explored the spin-mixing, orbital angular momenta, *g*-factors and Berry curvatures for several TMDCs with hexagonal crystal structure, namely MoS_2, $MoSe_2$, $MoTe_2$, WS_2 and WSe_2. Although our approach is quite general and it is valid for the entire Brillouin zone, we focused on the low energy bands, namely $VB_\pm$ and $CB_\pm$ (with the subindex $\pm$ referring to the energetic ordering of the spin-split bands). Surprisingly, our calculations revealed strong spin-mixing features at the *K*-valleys that are drastically enhanced by compressive strain, particularly for the low energy conduction band with $S_z < 0$, i.e., $CB_{+(-)}$ in Mo(W)-based compounds. Analyzing the symmetry of the relevant energy bands and the SOC Hamiltonian, we show that the main mechanism behind this strong reduction of S_z at the *K*-valley is an allowed spin-flip coupling between CB with spin-down and the higher-energy conduction band with spin-up. This result is particularly relevant to the spin dynamics of TMDCs, which can be strongly altered with strain.
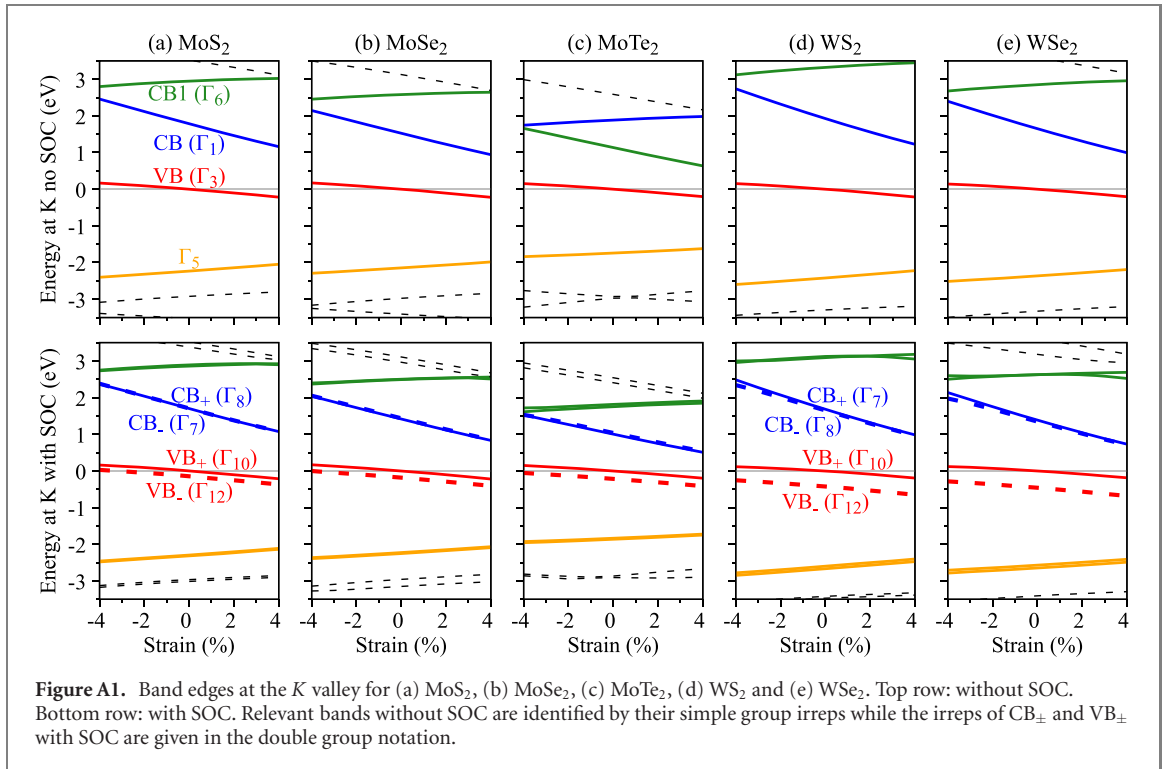
For direct excitons stemming from $VB_\pm$ and $CB_\pm$ at the *K*-valleys (A, B and D excitons), our calculations show that positive (negative) strain values increase (decrease) the absolute value of the *g*-factors, which are responsible for the observed valley Zeeman splitting in magneto optics experiments. Interestingly, we found that g_A and g_B split for compressive strain and g_D is the most sensitive *g*-factor with respect to the applied strain. Furthermore, our findings suggest that strain effects are one of the sources of uncertainty in the available experimental data of *g*-factors, i.e., strain variations of $\pm 0.5\%$ can modify the A and B bright excitons *g*-factors by ~ 0.3 (0.2) for W (Mo) based compounds and the dark exciton *g*-factors by ~ 0.5 (0.3) for W (Mo) compounds. We emphasize that, at zero strain, our *g*-factor calculations are in great agreement with the available experimental data. For a better insight into the exciton *g*-factor trends under strain we also analyzed the dipole matrix elements. Surprisingly, we found that in the regime of compressive strain, where the mixing of S_z is getting stronger, the dark exciton gets brighter (the out-of-plane selection rule still holds). These changes in the dark exciton matrix elements vary by orders of magnitude for a few percent strain. Additionally, by comparing different TMDC materials we can probe the signatures of the SOC in the spin and orbital angular momenta. We found that the larger the SOC, the larger the changes in spin, orbital angular momenta and *g*-factors. Therefore, monolayer WSe_2 seems to be the ideal candidate to explore the influence of strain on the spin-valley physics.

We have also looked at the points outside the *K*-valley that could also be affected by strain, i.e., the Γ and *Q* points. In general, these side points are highly spin polarized ($S_z \sim 1$) but show a small, or even negligible, orbital angular momenta contribution. Furthermore, we also complement our analysis by looking at the Berry curvatures. They display similar trends as the *g*-factors but are more sensitive to strain variations. Outside the *K*-valleys, the Berry curvature is strongly suppressed and we speculate that under strain, the direct to indirect band gap transition could be indirectly probed by abrupt changes in the Hall conductivity.

Finally, we emphasize that our study establishes the isolated impact of strain in the spin-valley properties of monolayers TMDCs. Besides the valuable insight for interpreting experiments in these systems, in which many effects (such as doping, temperature, dielectric screening, etc) are possibly competing with strain, our results are also relevant for investigations of proximity effects and interlayer excitons in TMDC-based van der Waals heterostructures.

Figure A1. Band edges at the K valley for (a) MoS$_2$, (b) MoSe$_2$, (c) MoTe$_2$, (d) WS$_2$ and (e) WSe$_2$. Top row: without SOC. Bottom row: with SOC. Relevant bands without SOC are identified by their simple group irreps while the irreps of CB$_\pm$ and VB$_\pm$ with SOC are given in the double group notation.

Appendix A.　Energies and irreducible representations at the K-valleys

The irreducible representations (irreps) given in figure A1 follow the notation of Koster *et al* [146] for the symmetry group C_{3h}.

Appendix B.　Symmetry analysis of the spin−orbit coupling at the K-valley

In this section, we elaborate on the mechanism behind the drastic reduction of S_z in the conduction band with $S_z < 0$ (CB$_+$ in Mo-based materials and CB$_-$ in W-based materials). To understand this mechanism we need to evaluate the matrix elements of the SOC Hamiltonian, given by

$$
\begin{aligned}
\mathbf{H_{SO}} &= \frac{\hbar}{4m_0^2 c^2}\left(\vec{\nabla}V \times \vec{p}\right)\cdot\vec{\sigma} \\
&= \frac{\hbar}{4m_0^2 c^2}\left[\left(\frac{\partial V}{\partial y}p_z - \frac{\partial V}{\partial z}p_y\right)\sigma_x + \left(\frac{\partial V}{\partial z}p_x - \frac{\partial V}{\partial x}p_z\right)\sigma_y \right.\\
&\quad \left. + \left(\frac{\partial V}{\partial x}p_y - \frac{\partial V}{\partial y}p_x\right)\sigma_z\right] \\
&= H_{SOx}\sigma_x + H_{SOy}\sigma_y + H_{SOz}\sigma_z.
\end{aligned}
\tag{B.1}
$$

The relevant matrix elements between states α and α' can be summarized as follows

$$
\begin{aligned}
\langle\alpha\uparrow|\mathbf{H_{SO}}|\alpha'\uparrow\rangle &= \langle\alpha|H_{SOz}|\alpha'\rangle \\
\langle\alpha\downarrow|\mathbf{H_{SO}}|\alpha'\downarrow\rangle &= -\langle\alpha|H_{SOz}|\alpha'\rangle \\
\langle\alpha\uparrow|\mathbf{H_{SO}}|\alpha'\downarrow\rangle &= \langle\alpha|H_{SO-}|\alpha'\rangle \\
\langle\alpha\downarrow|\mathbf{H_{SO}}|\alpha'\uparrow\rangle &= \langle\alpha|H_{SO+}|\alpha'\rangle
\end{aligned}
\tag{B.2}
$$

Table B1. Allowed coupling for the matrix element $\langle\alpha|R_{+,-,z}|\alpha'\rangle \sim \Gamma^*(\alpha) \otimes \Gamma(R_{+,-,z}) \otimes \Gamma(\alpha')$.

	Γ_1	Γ_2	Γ_3	Γ_4	Γ_5	Γ_6
Γ_1	R_z				R_-	R_+
Γ_2			R_z	R_-	R_+	
Γ_3		R_z		R_+		R_-
Γ_4		R_-	R_+	R_z		
Γ_5	R_-	R_+				R_z
Γ_6	R_+		R_-		R_z	

with $H_{SO\pm} = H_{SOx} \pm iH_{SOy}$, $H_{SO+} \sim R_+ \sim \Gamma_5$, $H_{SO-} \sim R_- \sim \Gamma_6$, $H_{SOz} \sim R_z \sim \Gamma_1$, with $R_{+,-,z}$ representing the pseudo-vector operators within the symmetry group. The irreps of the SOC operators also follow the notation of Koster *et al* [146] for the symmetry group C_{3h}.

Considering α and α' belonging to the simple group, i.e., $\{\alpha, \alpha'\} = \{\Gamma_1, \ldots, \Gamma_6\}$, the allowed symmetry couplings for $H_{SO\pm}$ and H_{SOz} can be summarized in table B1.

From this general symmetry analysis, presented in table B1, we can already draw important conclusions. At the K-valleys, in the presence of SOC:

- Every band will be split (via the intraband term H_{SOz}). This gives rise to the two energetically distinct spin branches, for instance, CB$_\pm$ and VB$_\pm$. Furthermore, if any pair of bands at the K-valleys are degenerate, it is an *accidental degeneracy*.

- Every band shows a coupling with some other band via the interband term $H_{SO\pm}$, i.e., the spin-flip SOC term. Therefore, every band at the K point in a TMDC monolayer is a spin-mixed state. The relevant question one should ask is then: *how large is the spin mixing?*

Let us restrict ourselves to the particular case we are interested in, i.e., analyze the role of the SOC in the spin-mixing of CB ($\sim\Gamma_1$) due to the presence of a higher conduction band CB1 ($\sim\Gamma_6$). We need to evaluate the following matrix elements

$$\langle CB\downarrow|\mathbf{H_{SO}}|CB1\uparrow\rangle = \langle\Gamma_1|H_{SO+}|\Gamma_6\rangle$$

$$\sim \Gamma_1^* \otimes (\Gamma_5 \otimes \Gamma_6)$$

$$= \Gamma_1 \otimes \Gamma_1$$

$$= \Gamma_1 \Rightarrow \text{ALLOWED}$$

$$\langle CB\uparrow|\mathbf{H_{SO}}|CB1\downarrow\rangle = \langle\Gamma_1|H_{SO-}|\Gamma_6\rangle$$

$$\sim \Gamma_1^* \otimes (\Gamma_6 \otimes \Gamma_6)$$

$$= \Gamma_1 \otimes \Gamma_2$$

$$= \Gamma_2 \Rightarrow \text{FORBIDDEN}, \tag{B.3}$$

which reveals that only the spin-down ($S_z < 0$) branch of CB is modified. This effect is drastically enhanced when CB and CB1 are brought energetically closer to each other via compressive strain, as shown in figure A1.

Appendix C. Spin, orbital angular momentum and *g*-factors at the *K*-valley for all TMDCs

In figure C1 we present the calculated values of S_z, L_z, and g_z as function of strain for all studied TMDCs.

Appendix D. Zero strain properties of VB$_\pm$ and CB$_\pm$ for all TMDCs

In table D1, we present the SOC splittings for conduction and valence bands. In tables D2–D5, we present the values of S_z, L_z, g_z, and Ω_z, respectively, at zero strain.
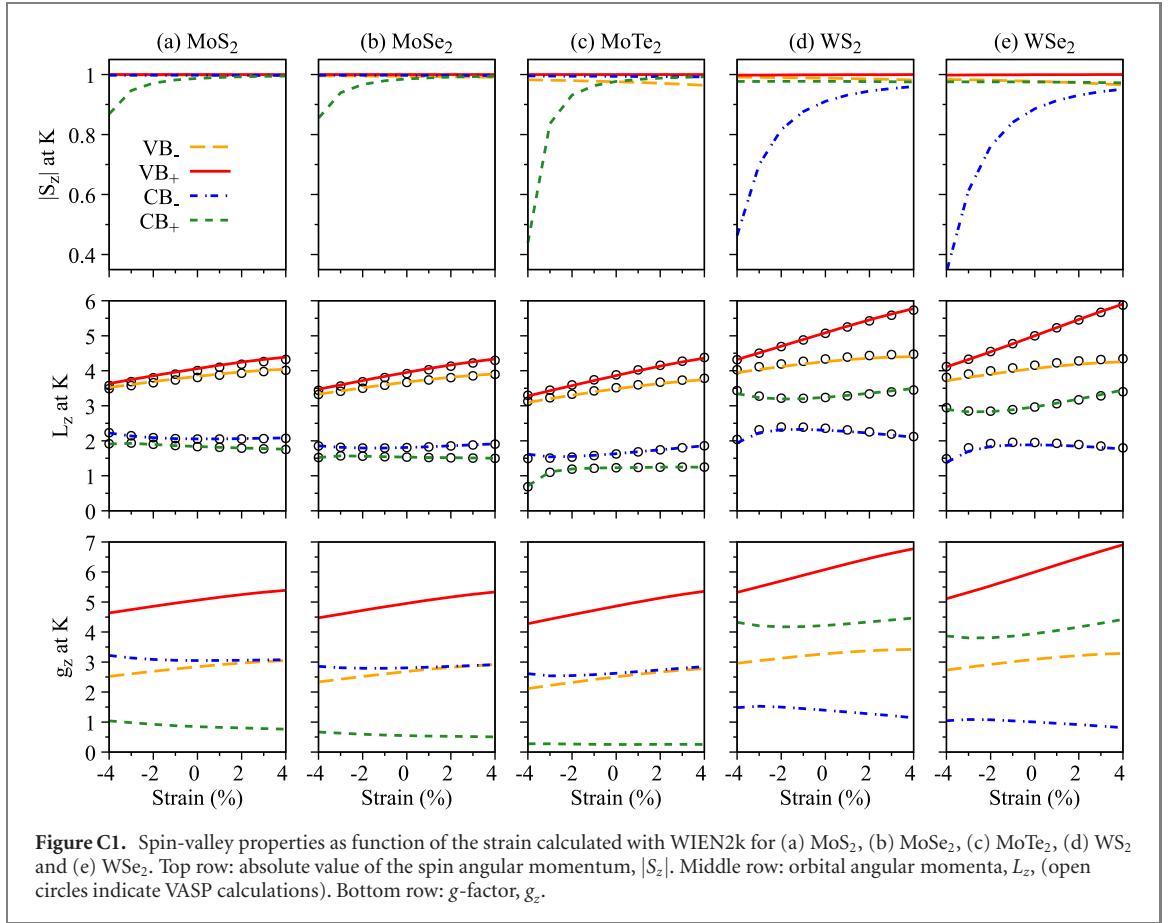
Figure C1. Spin-valley properties as function of the strain calculated with WIEN2k for (a) MoS$_2$, (b) MoSe$_2$, (c) MoTe$_2$, (d) WS$_2$ and (e) WSe$_2$. Top row: absolute value of the spin angular momentum, $|S_z|$. Middle row: orbital angular momenta, L_z, (open circles indicate VASP calculations). Bottom row: g-factor, g_z.

Table D1. Conduction, Δ_{cb}, and valence, Δ_{vb}, band splittings in meV. Negative values of Δ_{cb} indicate spin up below spin down (see figure 2).

	MoS$_2$	MoSe$_2$	MoTe$_2$	WS$_2$	WSe$_2$
Δ_{cb}	−2.3	−20.8	−34.0	34.0	39.2
Δ_{vb}	146.2	184.1	215.4	278.7	460.0

Table D2. Spin angular momenta, S_z.

S_z	VB$_-$	VB$_+$	CB$_-$	CB$_+$
MoS$_2$	−0.9982	0.9999	0.9974	−0.9872
MoSe$_2$	−0.9938	1.0000	0.9973	−0.9853
MoTe$_2$	−0.9760	1.0000	0.9939	−0.9768
WS$_2$	−0.9879	0.9990	−0.9106	0.9771
WSe$_2$	−0.9772	0.9992	−0.8856	0.9752

Table D3. Orbital angular momenta, L_z.

L_z	VB$_-$	VB$_+$	CB$_-$	CB$_+$
MoS$_2$	3.8414	4.0649	2.0540	1.8352
MoSe$_2$	3.6793	3.9557	1.8079	1.5317
MoTe$_2$	3.4840	3.8634	1.6314	1.2312
WS$_2$	4.2623	5.0863	2.3039	3.2397
WSe$_2$	4.0662	5.0001	1.8863	2.9694

Table D4. Band *g*-factor, g_z.

g_z	VB$_-$	VB$_+$	CB$_-$	CB$_+$
MoS$_2$	2.8432	5.0648	3.0514	0.8480
MoSe$_2$	2.6855	4.9557	2.8052	0.5464
MoTe$_2$	2.5080	4.8634	2.6253	0.2544
WS$_2$	3.2744	6.0853	1.3933	4.2168
WSe$_2$	3.0890	5.9993	1.0007	3.9446

Table D5. Berry curvature, Ω_z, given in Å^2.

		VB$_-$	VB$_+$	CB$_-$	CB$_+$
	This study[a]	−7.9735	−9.6322	8.3757	6.7844
MoS$_2$	Reference [140][b]	−8.85	−10.87	9.98	5.27
	Reference [13][b]	−8.26	−9.88	9.88	8.26
	Reference [41][a]	−8.89	−10.90	8.00	9.97
	This study[a]	−8.2522	−10.8530	9.8532	7.3299
MoSe$_2$	Reference [140][a]	−8.40	−11.12	10.31	7.65
	Reference [13][b]	−7.96	−10.23	10.23	7.96
MoTe$_2$	This study[a]	−9.6985	−14.7353	13.7076	8.9063
	This study[a]	−9.3216	−15.3711	7.8584	13.6838
WS$_2$	Reference [140][a]	−9.77	−16.75	8.68	15.32
	Reference [13][b]	−9.57	−15.51	9.57	15.51
	This study[a]	−9.6323	−17.8521	8.3405	16.3563
WSe$_2$	Reference [140][a]	−9.72	−18.01	8.63	16.58
	Reference [13][b]	−9.39	−16.81	9.39	16.81

[a]First-principles.
[b]Two-band model.

Table E1. Comparison of the *g*-factors calculated with a zero and nonzero scissor (denote as sc. in the table) shift of 0.8 eV to increase the DFT band gap close to experimental values [19]. The values in parenthesis for the experimental studies are the exciton *g*-factors calculated from the band *g*-factors determined experimentally for VB$_\pm$ and CB$_\pm$.
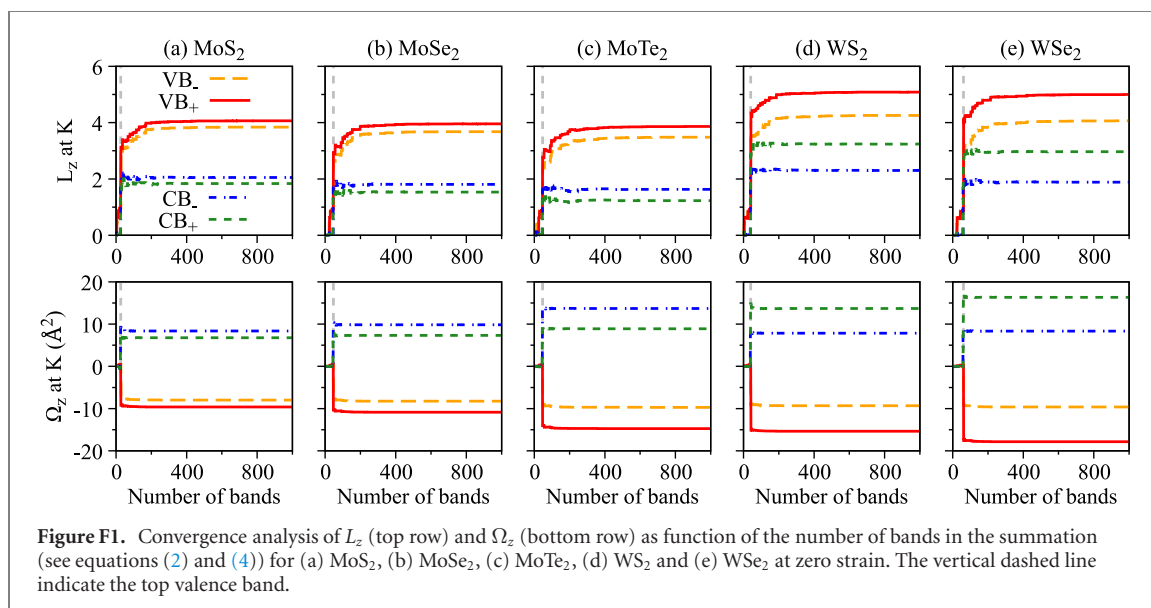
		VB$_-$	VB$_+$	CB$_-$	CB$_+$	g_A	g_B	g_D
	No sc.	3.0890	5.9993	1.0007	3.9446	−4.1094	−4.1766	−9.9972
WSe$_2$	With sc.	2.3501	4.7746	0.3706	2.8198	−3.9096	−3.9590	−8.8080
	Exp. [33]	2.81 ± 0.5	6.1 ± 0.1	0.86 ± 0.1	3.84 ± 0.1	−4.5 ± 0.1	−3.9 ± 0.5	−10.2 ± 0.1
	No sc.	3.2744	6.0853	1.3933	4.2168	−3.7370	−3.7622	−9.3840
WS$_2$	With sc.	2.5301	4.9551	0.7466	3.1795	−3.5512	−3.5670	−8.4170
	Exp. [34]	3.08 ± 0.08	5.47 ± 0.09	1.08 ± 0.08	3.70 ± 0.10	−3.5 ± 0.1		−8.9 ± 0.1

Appendix E. Impact of scissor shift in the *g*-factors

The impact of a scissor shift in the calculated *g*-factors of WSe$_2$ and WS$_2$ is shown in table E1.

Appendix F. Convergence of L_z and Ω_z

In figure F1 we present the convergence with respect to the number of bands for L_z, and Ω_z at zero strain for all studied TMDCs. For nonzero strain values, convergence is also satisfied.

Figure F1. Convergence analysis of L_z (top row) and Ω_z (bottom row) as function of the number of bands in the summation (see equations (2) and (4)) for (a) MoS_2, (b) $MoSe_2$, (c) $MoTe_2$, (d) WS_2 and (e) WSe_2 at zero strain. The vertical dashed line indicate the top valence band.

ORCID iDs

Paulo E Faria Junior ⓘ https://orcid.org/0000-0002-1161-2059
Klaus Zollner ⓘ https://orcid.org/0000-0002-6239-3271
Tomasz Woźniak ⓘ https://orcid.org/0000-0002-2290-5738
Marcin Kurpas ⓘ https://orcid.org/0000-0002-9836-4173
Martin Gmitra ⓘ https://orcid.org/0000-0003-1118-3028
Jaroslav Fabian ⓘ https://orcid.org/0000-0002-3009-4525

References

[1] Jones A M *et al* 2013 *Nat. Nanotechnol.* **8** 634
[2] Ross J S *et al* 2014 *Nat. Nanotechnol.* **9** 268
[3] Mak K F and Shan J 2016 *Nat. Photon.* **10** 216
[4] Gmitra M and Fabian J 2015 *Phys. Rev. B* **92** 155403
[5] Luo Y K, Xu J, Zhu T, Wu G, McCormick E J, Zhan W, Neupane M R and Kawakami R K 2017 *Nano Lett.* **17** 3877
[6] Avsar A, Unuchek D, Liu J, Sanchez O L, Watanabe K, Taniguchi T, Özyilmaz B and Kis A 2017 *ACS Nano* **11** 11678
[7] Mak K F, He K, Shan J and Heinz T F 2012 *Nat. Nanotechnol.* **7** 494
[8] Mak K F, McGill K L, Park J and McEuen P L 2014 *Science* **344** 1489
[9] Xu X, Yao W, Xiao D and Heinz T F 2014 *Nat. Phys.* **10** 343
[10] Schaibley J R, Yu H, Clark G, Rivera P, Ross J S, Seyler K L, Yao W and Xu X 2016 *Nat. Rev. Mater.* **1** 16055
[11] Kuc A, Zibouche N and Heine T 2011 *Phys. Rev. B* **83** 245213
[12] Kumar A and Ahluwalia P K 2012 *Eur. Phys. J. B* **85** 186
[13] Xiao D, Liu G-B, Feng W, Xu X and Yao W 2012 *Phys. Rev. Lett.* **108** 196802
[14] Mak K F, Lee C, Hone J, Shan J and Heinz T F 2010 *Phys. Rev. Lett.* **105** 136805
[15] Splendiani A, Sun L, Zhang Y, Li T, Kim J, Chim C-Y, Galli G and Wang F 2010 *Nano Lett.* **10** 1271
[16] Chernikov A, Berkelbach T C, Hill H M, Rigosi A, Li Y, Aslan O B, Reichman D R, Hybertsen M S and Heinz T F 2014 *Phys. Rev. Lett.* **113** 076802
[17] Wang G, Chernikov A, Glazov M M, Heinz T F, Marie X, Amand T and Urbaszek B 2018 *Rev. Mod. Phys.* **90** 021001
[18] Raja A *et al* 2017 *Nat. Commun.* **8** 15251
[19] Kormányos A, Burkard G, Gmitra M, Fabian J, Zólyomi V, Drummond N D and Fal'ko V 2015 *2D Mater.* **2** 022001
[20] Kurpas M, Faria Junior P E, Gmitra M and Fabian J 2019 *Phys. Rev. B* **100** 125422
[21] Arora A 2021 *J. Appl. Phys.* **129** 120902
[22] Li Y *et al* 2014 *Phys. Rev. Lett.* **113** 266804
[23] MacNeill D, Heikes C, Mak K F, Anderson Z, Kormányos A, Zólyomi V, Park J and Ralph D C 2015 *Phys. Rev. Lett.* **114** 037401
[24] Srivastava A, Sidler M, Allain A V, Lembke D S, Kis A and Imamoğlu A 2015 *Nat. Phys.* **11** 141
[25] Aivazian G *et al* 2015 *Nat. Phys.* **11** 148
[26] Wang G, Bouet L, Glazov M M, Amand T, Ivchenko E L, Palleau E, Marie X and Urbaszek B 2015 *2D Mater.* **2** 034002
[27] Mitioglu A A, Plochocka P, Granados del Aguila Á, Christianen P C M, Deligeorgis G, Anghel S, Kulyuk L and Maude D K 2015 *Nano Lett.* **15** 4387
[28] Stier A V, McCreary K M, Jonker B T, Kono J and Crooker S A 2016 *Nat. Commun.* **7** 10643
[29] Plechinger G *et al* 2016 *Nano Lett.* **16** 7899
[30] Zipfel J *et al* 2018 *Phys. Rev. B* **98** 075438
[31] Stier A V, Wilson N P, Velizhanin K A, Kono J, Xu X and Crooker S A 2018 *Phys. Rev. Lett.* **120** 057405
[32] Goryca M *et al* 2019 *Nat. Commun.* **10** 4172
[33] Robert C *et al* 2021 *Phys. Rev. Lett.* **126** 067403

[34] Zinkiewicz M *et al* 2021 *Nano Lett.* **21** 2519
[35] Robert C *et al* 2020 *Nat. Commun.* **11** 4037
[36] Robert C *et al* 2017 *Phys. Rev.* B **96** 155423
[37] Molas M R *et al* 2019 *Phys. Rev. Lett.* **123** 096803
[38] Woźniak T, Faria Junior P E, Seifert G, Chaves A and Kunstmann J 2020 *Phys. Rev.* B **101** 235408
[39] Deilmann T, Krüger P and Rohlfing M 2020 *Phys. Rev. Lett.* **124** 226402
[40] Förste J *et al* 2020 *Nat. Commun.* **11** 4539
[41] Xuan F and Quek S Y 2020 *Phys. Rev. Res.* **2** 033256
[42] Luttinger J M and Kohn W 1955 *Phys. Rev.* **97** 869
[43] Luttinger J M 1956 *Phys. Rev.* **102** 1030
[44] Kohn W 1959 *Phys. Rev.* **115** 1460
[45] Roth L M, Lax B and Zwerdling S 1959 *Phys. Rev.* **114** 90
[46] Roth L M 1960 *Phys. Rev.* **118** 1534
[47] Roth L M 1962 *J. Phys. Chem. Solids* **23** 433
[48] Hermann C and Weisbuch C 1977 *Phys. Rev.* B **15** 823
[49] Alegre T P M, Hernández F G G, Pereira A L C and Medeiros-Ribeiro G 2006 *Phys. Rev. Lett.* **97** 236402
[50] Bastos C M O, Sabino F P, Sipahi G M and Da Silva J L F 2018 *J. Appl. Phys.* **123** 065702
[51] Faria Junior P E, Tedeschi D, De Luca M, Scharf B, Polimeni A and Fabian J 2019 *Phys. Rev.* B **99** 195205
[52] Gawarecki K and Zieliński M 2020 *Sci. Rep.* **10** 22001
[53] Xuan F and Quek S Y 2021 *npj Comput. Mater.* **7** 198
[54] Amit T, Hernangómez-Pérez D, Cohen G, Qiu D Y and Refaely-Abramson S 2022 arXiv:2203.14125
[55] Raiber S, Faria Junior P E, Falter D, Feldl S, Marzena P, Watanabe K, Taniguchi T, Fabian J and Schüller C 2022 arXiv:2204.12343
[56] Akinwande D, Petrone N and Hone J 2014 *Nat. Commun.* **5** 5678
[57] Miao F, Liang S J and Cheng B 2021 *npj Quantum Mater.* **6** 59
[58] Plechinger G, Castellanos-Gomez A, Buscema M, van der Zant H S J, Steele G A, Kuc A, Heine T, Schüller C and Korn T 2015 *2D Mater.* **2** 015006
[59] Schmidt R, Niehues I, Schneider R, Drüppel M, Deilmann T, Rohlfing M, De Vasconcellos S M, Castellanos-Gomez A and Bratschitsch R 2016 *2D Mater.* **3** 021011
[60] Lloyd D, Liu X, Christopher J W, Cantley L, Wadehra A, Kim B L, Goldberg B B, Swan A K and Bunch J S 2016 *Nano Lett.* **16** 5836
[61] Blundo E *et al* 2020 *Phys. Rev. Res.* **2** 012024
[62] Dirnberger F *et al* 2021 *Sci. Adv.* **7** eabj3066
[63] Blundo E, Cappelluti E, Felici M, Pettinari G and Polimeni A 2021 *Appl. Phys. Rev.* **8** 021318
[64] Kim H, Uddin S Z, Higashitarumizu N, Rabani E and Javey A 2021 *Science* **373** 448
[65] Mennel L, Furchi M M, Wachter S, Paur M, Polyushkin D K and Mueller T 2018 *Nat. Commun.* **9** 516
[66] Trainer D J, Zhang Y, Bobba F, Xi X, Hla S-W and Iavarone M 2019 *ACS Nano* **13** 8284
[67] Kolesnichenko P V, Zhang Q, Yun T, Zheng C, Fuhrer M S and Davis J A 2020 *2D Mater.* **7** 025008
[68] Darlington T P *et al* 2020 *Nat. Nanotechnol.* **15** 854
[69] Alexeev E M *et al* 2020 *ACS Nano* **14** 11110
[70] Peelaers H and Van de Walle C G 2012 *Phys. Rev.* B **86** 241401
[71] Johari P and Shenoy V B 2012 *ACS Nano* **6** 5449
[72] Frisenda R, Drüppel M, Schmidt R, Michaelis de Vasconcellos S, Perez de Lara D, Bratschitsch R, Rohlfing M and Castellanos-Gomez A 2017 *npj 2D Mater. Appl.* **1** 10
[73] Zollner K, Faria Junior P E and Fabian J 2019 *Phys. Rev.* B **100** 195126
[74] Gmitra M, Kochan D, Högl P and Fabian J 2016 *Phys. Rev.* B **93** 155104
[75] Tran K, Choi J and Singh A 2020 *2D Mater.* **8** 022002
[76] Slobodkin Y, Mazuz-Harpaz Y, Refaely-Abramson S, Gazit S, Steinberg H and Rapaport R 2020 *Phys. Rev. Lett.* **125** 255301
[77] Plankl M *et al* 2021 *Nat. Photon.* **15** 594
[78] Sierra J F, Fabian J, Kawakami R K, Roche S and Valenzuela S O 2021 *Nat. Nanotechnol.* **16** 856
[79] Brotons-Gisbert M, Baek H, Campbell A, Watanabe K, Taniguchi T and Gerardot B D 2021 *Phys. Rev.* X **11** 031033
[80] Mahdikhanysarvejahany F *et al* 2021 *npj 2D Mater. Appl.* **5** 67
[81] Naimer T, Zollner K, Gmitra M and Fabian J 2021 *Phys. Rev.* B **104** 195156
[82] Halbertal D, Shabani S, Passupathy A N and Basov D N 2022 *ACS Nano* **16** 1471−6
[83] Gobato Y G *et al* 2022 arXiv:2204.01813
[84] Chang M-C and Niu Q 1996 *Phys. Rev.* B **53** 7010
[85] Xiao D, Chang M-C and Niu Q 2010 *Rev. Mod. Phys.* **82** 1959
[86] Nagaosa N, Sinova J, Onoda S, MacDonald A H and Ong N P 2010 *Rev. Mod. Phys.* **82** 1539
[87] Srivastava A and Imamoğlu A 2015 *Phys. Rev. Lett.* **115** 166802
[88] Zhou J, Shan W-Y, Yao W and Xiao D 2015 *Phys. Rev. Lett.* **115** 166803
[89] Wu F, Qu F and MacDonald A H 2015 *Phys. Rev.* B **91** 075310
[90] Nye J F 1985 *Physical Properties of Crystals: Their Representation by Tensors and Matrices* (Oxford: Oxford University Press)
[91] Dresselhaus M S, Dresselhaus G and Jorio A 2007 *Group Theory: Application to the Physics of Condensed Matter* (Berlin: Springer)
[92] Cooper R C, Lee C, Marianetti C A, Wei X, Hone J and Kysar J W 2013 *Phys. Rev.* B **87** 035423
[93] Duerloo K-A N, Ong M T and Reed E J 2012 *J. Phys. Chem. Lett.* **3** 2871
[94] Blaha P, Schwarz K, Tran F, Laskowski R, Madsen G K H and Marks L D 2020 *J. Chem. Phys.* **152** 074101
[95] Larsen A H *et al* 2017 *J. Phys.: Condens. Matter.* **29** 273002
[96] Perdew J P, Burke K and Ernzerhof M 1996 *Phys. Rev. Lett.* **77** 3865
[97] Singh D J and Nordstrom L 2006 *Planewaves, Pseudopotentials, and the LAPW Method* (New York: Springer)
[98] Kresse G and Furthmüller J 1996 *Phys. Rev.* B **54** 11169
[99] Kresse G and Joubert D 1999 *Phys. Rev.* B **59** 1758
[100] Gajdoš M, Hummer K, Kresse G, Furthmüller J and Bechstedt F 2006 *Phys. Rev.* B **73** 045112

[101] Qiu D Y, da Jornada F H and Louie S G 2013 *Phys. Rev. Lett.* **111** 216805

[102] Li Y *et al* 2014 *Phys. Rev.* B **90** 205422

[103] Kapuściński P *et al* 2021 *Commun. Phys.* **4** 186

[104] Xiao D, Yao W and Niu Q 2007 *Phys. Rev. Lett.* **99** 236809

[105] Dey P, Yang L, Robert C, Wang G, Urbaszek B, Marie X and Crooker S A 2017 *Phys. Rev. Lett.* **119** 137401

[106] Li J, Goryca M, Yumigeta K, Li H, Tongay S and Crooker S A 2021 *Phys. Rev. Mater.* **5** 044001

[107] Kumar A, Yagodkin D, Stetzuhn N, Kovalchuk S, Melnikov A, Elliott P, Sharma S, Gahl C and Bolotin K I 2021 *Nano Lett.* **21** 7123

[108] Zollner K, Faria Junior P E and Fabian J 2019 *Phys. Rev.* B **100** 085128

[109] Zollner K, Gmitra M and Fabian J 2020 *Phys. Rev. Lett.* **125** 196402

[110] Rohlfing M and Louie S G 2000 *Phys. Rev.* B **62** 4927

[111] Faria Junior P E, Kurpas M, Gmitra M and Fabian J 2019 *Phys. Rev.* B **100** 115203

[112] Lin K-Q *et al* 2021 *Nat. Commun.* **12** 5500

[113] Caruso F, Schebek M, Pan Y, Vona C and Draxl C 2021 arXiv:2112.04781

[114] Mitioglu A, Buhot J, Ballottin M V, Anghel S, Sushkevich K, Kulyuk L and Christianen P C M 2018 *Phys. Rev.* B **98** 235429

[115] Covre F S *et al* 2022 *Nanoscale* **14** 5758

[116] Klein J *et al* 2021 *Phys. Rev. Res.* **3** L022009

[117] Cadiz F *et al* 2017 *Phys. Rev.* X **7** 021026

[118] Mitioglu A A, Galkowski K, Surrente A, Klopotowski L, Dumcenco D, Kis A, Maude D K and Plochocka P 2016 *Phys. Rev.* B **93** 165412

[119] Koperski M, Molas M R, Arora A, Nogajewski K, Bartos M, Wyzula J, Vaclavkova D, Kossacki P and Potemski M 2018 *2D Mater.* **6** 015001

[120] Arora A *et al* 2018 *2D Mater.* **6** 015010

[121] Arora A, Schmidt R, Schneider R, Molas M R, Breslavetz I, Potemski M and Bratschitsch R 2016 *Nano Lett.* **16** 3624

[122] Prando G A, Severijnen M E, Barcelos I D, Zeitler U, Christianen P C M, Withers F and Galvão Gobato Y 2021 *Phys. Rev. Appl.* **16** 064055

[123] Kuhnert J, Rahimi-Iman A and Heimbrodt W 2017 *J. Phys.: Condens. Matter.* **29** 08LT02

[124] Schmidt R *et al* 2016 *Phys. Rev. Lett.* **117** 077402

[125] Koperski M, Nogajewski K, Arora A, Cherkez V, Mallet P, Veuillen J-Y, Marcus J, Kossacki P and Potemski M 2015 *Nat. Nanotechnol.* **10** 503

[126] Li Z *et al* 2019 *ACS Nano* **13** 14107

[127] Li Z *et al* 2019 *Nat. Commun.* **10** 2469

[128] Stier A V, Wilson N P, Clark G, Xu X and Crooker S A 2016 *Nano Lett.* **16** 7054

[129] Chen S-Y *et al* 2019 *Nano Lett.* **19** 2464

[130] Liu E, van Baren J, Lu Z, Altaiary M M, Taniguchi T, Watanabe K, Smirnov D and Lui C H 2019 *Phys. Rev. Lett.* **123** 027401

[131] He M *et al* 2020 *Nat. Commun.* **11** 618

[132] Liu E, van Baren J, Taniguchi T, Watanabe K, Chang Y C and Lui C H 2019 *Phys. Rev. Res.* **1** 032007

[133] Feierabend M, Khatibi Z, Berghäuser G and Malic E 2019 *Phys. Rev.* B **99** 195454

[134] Feierabend M, Brem S, Ekman A and Malic E 2020 *2D Mater.* **8** 015013

[135] Ghorbani-Asl M, Borini S, Kuc A and Heine T 2013 *Phys. Rev.* B **87** 235434

[136] Shi H, Pan H, Zhang Y-W and Yakobson B I 2013 *Phys. Rev.* B **87** 155304

[137] Chang C H, Fan X, Lin S H and Kuo J L 2013 *Phys. Rev.* B **88** 195420

[138] Amin B, Kaloni T P and Schwingenschlögl U 2014 *RSC Adv.* **4** 34561

[139] Ortenzi L, Pietronero L and Cappelluti E 2018 *Phys. Rev.* B **98** 195313

[140] Feng W, Yao Y, Zhu W, Zhou J, Yao W and Xiao D 2012 *Phys. Rev.* B **86** 165108

[141] Son J, Kim K H, Ahn Y H, Lee H W and Lee J 2019 *Phys. Rev. Lett.* **123** 036806

[142] Cysne T P, Costa M, Canonico L M, Nardelli M B, Muniz R B and Rappoport T G 2021 *Phys. Rev. Lett.* **126** 056601

[143] Bhowal S and Vignale G 2021 *Phys. Rev.* B **103** 195309

[144] Chaudhary S, Knapp C and Refael G 2021 *Phys. Rev.* B **103** 165119

[145] Cao J, Fertig H A and Brey L 2021 *Phys. Rev.* B **103** 115422

[146] Koster G F, Dimmock J O and Wheeler R G 1963 *Properties of the Thirty-Two Point Groups* vol 24 (Cambridge, MA: MIT Press)